

THE EFFECTS OF METALLICITY AND GRAIN SIZE ON GRAVITATIONAL INSTABILITIES IN PROTOPLANETARY DISKS. Kai Cai (kai@astro.indiana.edu), Richard H. Durisen, Scott Michael, Aaron C. Boley, *Astronomy Department, Indiana University, Bloomington, IN 47405*, Annie C. Mejía, *Department of Astronomy, University of Washington, Box 351580, Seattle, WA 98195-1580*, Megan K. Pickett, *Department of Chemistry and Physics, Purdue University Calumet, 2200 169th St., Hammond, IN 46410*, Paola D’Alessio, *Centro de Radioastronomía y de Astrofísica, Apartado Postal 72-3, 58089 Morelia, Michoacan, Mexico.*

Introduction: Observational studies of exoplanets show that the probability of finding a planet around a star increases with the host star’s metallicity [1, 2]. This trend suggests that metal-rich protoplanetary disks are more conducive to gas giant planet formation than their metal-poor counterparts. Calculations show that this trend can probably be explained within the framework of the core accretion scenario [3, 4]. On the other hand, in 3D hydrodynamics simulations with radiative cooling, Boss [5] finds that rapid cooling produces gravitational instabilities (GIs) strong enough to form protoplanetary clumps regardless of metallicity, and he [6] attributes the observed metallicity trend in planet detection to other causes. Using a different treatment of radiative cooling, which incorporates both optically thin and thick regions of the disk coupled by an Eddington-like atmosphere boundary condition, Mejía [7] sees longer cooling times (t_{cool}) and no persistent clumps in her simulations. Here we use Mejía’s methods to test whether GI strengths vary with metallicity and grain size.

Methods: We perform our disk simulations using the Indiana University 3D Hydrodynamics Group code [7, 8, 9]. We adopt the treatment of radiative physics in Mejía [7] but add irradiation by a 15K envelope that is approximated as shining vertically down on the disk [10]. The opacities and molecular weights used in our simulations are described in D’Alessio et al. [11]. As in Boss [5], the metallicity variation is modeled by multiplying the tabulated mean opacities by a factor $f_{\kappa} = Z/Z_{\odot}$, where Z is the metallicity (see Table 1).

Simulations: The initial axisymmetric model for all the calculations is the same one used by Mejía et al. [9]. It has a central star of $0.5 M_{\odot}$ and a disk of $0.07 M_{\odot}$, with surface density $\Sigma(r) \propto r^{-0.5}$ from 2.3 AU to 40 AU. The grid has an initial size in cylindrical coordinates of $(r, \phi, z) = (256, 128, 32)$ above the equatorial plane. A minimum value of the Toomre $Q \approx 1.5$ means that the disk is initially marginally unstable to GI’s (see [9]). As summarized in Table 1, we evolve the disk using four different metallicities: $1/4 Z_{\odot}$, $1/2 Z_{\odot}$, Z_{\odot} , $2 Z_{\odot}$. The $1/4 Z_{\odot}$ simulation is started from the $1/2 Z_{\odot}$ disk at 13.0 outer rotation periods (ORPs) to save computing resources. The ORP is defined as the initial rotation period at 33 AU, which is about 250 years. These four cases are done using a maximum grain size $a_{max} = 1 \mu\text{m}$. A fifth simulation with $a_{max} = 1 \text{ mm}$ and $Z = Z_{\odot}$ explores the effect of grain growth.

Results: As in Mejía [7] and Mejía et al. [9], these disks remain fairly axisymmetric until a *burst phase* of rapid GI growth. The disks then gradually transition into a quasi-steady state or *asymptotic phase*, where heating and cooling are in rough balance (see also [12]). The t_1 and t_2 in Table 1 mark the beginning of the burst phase and the asymptotic

phase, respectively. As in the radiative simulations presented in Mejía [7], no persistent dense clumps form in these simulations, but higher resolution tests are still underway. During the asymptotic phase, in all cases, the Toomre Q values are roughly constant at 1.3 to 1.8 between 10 to 40 AU and change little with time. The mass transport rates during this phase peak at $10^{-6} M_{\odot}/\text{yr}$, with no significant differences between the $1/2 Z_{\odot}$ and $2 Z_{\odot}$ runs.

Figure 1 shows that GI-generated structure is much stronger for $Z = 1/4 Z_{\odot}$ than for $Z = Z_{\odot}$. In order to quantify these differences, we compute a total amplitude for m -armed density structure [13]

$$A_m = \frac{\int \rho_m r dr dz}{\int \rho_0 r dr dz},$$

where ρ_0 is the axisymmetric component of density and ρ_m is the amplitude of the m th Fourier component of the density in the azimuthal direction. To measure total nonaxisymmetry, we sum the A_m ’s for $m = 2$ to 63 and average this sum from 14.5 to 15.5 ORPs. The resulting time-averaged sums are tabulated in Table 1 as $\langle A \rangle$. Clearly, $\langle A \rangle$ is greatest for $1/4 Z_{\odot}$ and decreases with increasing metallicity and increasing grain size. This, together with the fact that the burst is delayed in higher metallicity runs, indicates that, overall, lower metallicities and smaller grain size lead to more violent GI-activity.

In our simulations, GI’s behave as a global phenomenon, with transport dominated by low- m spiral modes [7, 8, 9]. During the asymptotic phase, we define a global cooling time by dividing the total internal energy of the disk by the total disk luminosity. As can be seen in Table 1, this overall t_{cool} is shorter for lower metallicity cases. For the 1mm case, outside the inner few AU, bigger grains make the disk more opaque to long wavelength radiation, and t_{cool} becomes even longer than for the highest metallicity case ($Z = 2 Z_{\odot}$). Differences between the total cooling rates are dominated by cooling in the optically thin regions, which Boss [5] does not treat explicitly. Substantial vertical entropy gradient inversions do occur in some cases, and we are investigating whether this signals the occurrence of thermal convection.

Discussion: Unlike Boss [5], our results show that the strength of GIs varies with metallicity and grain size in the sense that, overall, GIs become weaker as the opacity increases, a trend which runs counter to the observed correlation between metallicity and probability of planet detection. In all cases, our global cooling times are much longer than the value required for fragmentation of the disk, about half an orbit period according to Gammie [14]. However, we are still investigating whether shorter localized cooling times, possibly due to convection, might lead to fragmentation.

So far, our results seem to favor gas giant planet formation

by core accretion. Nevertheless, GIs may still play an important role. Dense gas rings produced by GIs in the inner disk may accelerate the growth of solid cores [15]. Such rings are produced in all our calculations and appear to be still growing when the calculations end (see Figure 1). If rings are present, then less energetic GIs mean that gravitoturbulence will cause less interference with the radial drift of solids into the rings [15]. In addition, rings provide a natural shelter for the growing solid cores by preventing loss of the cores into the star by rapid Type I migration. These effects may contribute to the connection between planet formation and metallicity.

L1551 IRS5 Disks: Recently, more and more disks in embedded star/disk systems are detectable with newly-equipped sub-millimeter instruments and interferometers. For instance, Osorio et al. [16] have studied the L1551 IRS5 binary system in unprecedented detail and estimated disk parameters based on fitting the observed fluxes with irradiated steady-state α -disk models. We will present preliminary results from a simulation of a disk based on their parameters. So far, we find that, although assessment of initial stability is complicated by strong irradiation and finite disk thickness [17, 18], the disk is in fact gravitationally unstable and develops a strong two-armed mode within a few rotation periods. The disk expands rapidly to a size approaching the Roche lobe radii in the system. The Osorio et al. models are thus not physically self-consistent for the L1551 IRS5 disks. Some more complex model accounting for the dynamical effects of GIs and system binarity are required.

Acknowledgments: This work was supported in part by NASA Origins of Solar Systems grant No. NAG5-11964, by NASA Planetary Geology and Geophysics grant No. NAG5-10262, and by a Shared University Research grants from IBM, Inc. to Indiana University.

References: [1] Santos, N. C., Israelian, G., & Mayor, M., 2001, A&A, 373, 1019. [2] Fischer, D.A., & Valenti, J., ApJ, 622, 1102. [3] Ida, S., & Lin, D.N.C., ApJ, 616, 567. [4] Kornet, K., Bodenheimer, P., Rózycka, M., & Stepinski, T. F., 2005, A&A, 430, 1133. [5] Boss, A.P., 2002, ApJ, 567, L149. [6] Boss, A.P., 2005, ApJ, 629, 535. [7] Mejía, A.C., Ph.D. dissertation, Indiana University. [8] Pickett, B. K., Mejía, A. C., Durisen, R. H., Cassen, P. M., Berry, D. K., & Link, R. P. 2003, ApJ, 590, 1060. [9] Mejía, A.C., Durisen, R.H., Pickett, M. K., & Cai, K., 2005, ApJ, 619, 1098. [10] Cai, K., Durisen, R.H., Michael, S., Boley, A.C., Mejía, A.C., Pickett, M.K., & D'Alessio, P., 2005, ApJL, in prep. [11] D'Alessio, P., Calvet, N., & Hartmann, L., 2001, ApJ, 553, 321. [12] Lodato, G., & Rice, W. K. M., 2005, MNRAS, 358, 1489. [13] Imamura, J. N., Durisen, R.H., & Pickett, B. K., 2000, ApJ, 528, 946. [14] Gammie, C.F., 2001, ApJ, 553, 174. [15] Durisen, R.H., Cai, K., Mejía, A.C., & Pickett, M.K., 2005, Icarus, 173, 417. [16] Osorio, M., D'Alessio, P., Muzerolle, J., Calvet, N., & Hartmann, L. 2003, ApJ 586, 1148. [17] Mayer, L., Quinn, T., Wadsley, J., Stadel, J., 2004 ApJ 609, 1045. [18] Romeo, A.B., 1992, MNRAS, 256, 307.

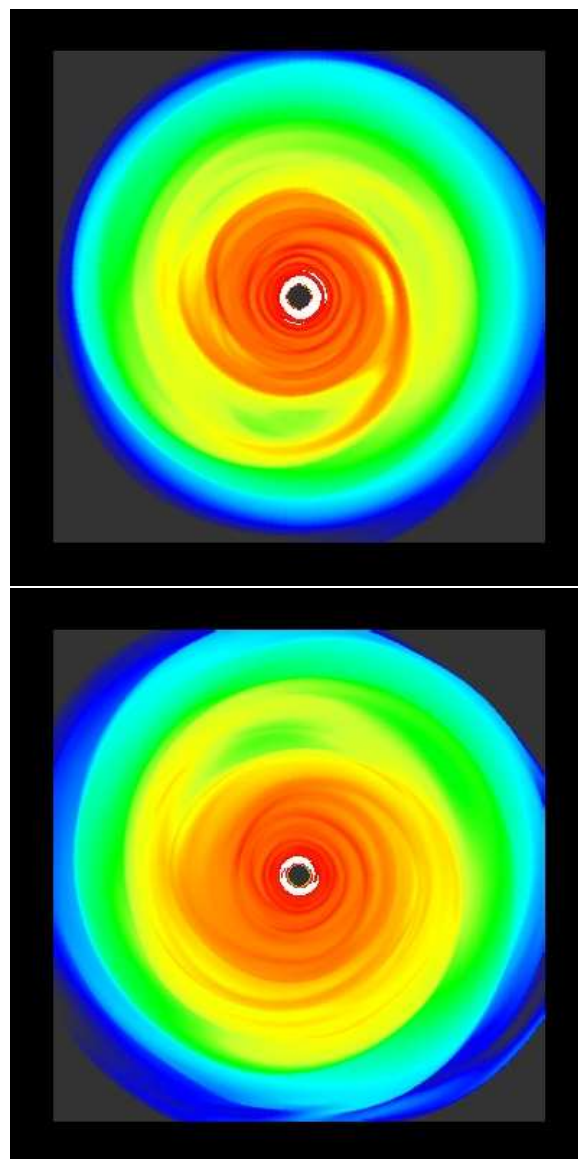


Figure 1: Midplane density maps at 15 ORPs for the $1/4 Z_{\odot}$ (top panel) and Z_{\odot} simulations near their ends. Each square is 113 AU on a side. Densities are displayed on a logarithmic scale from blue (low density) to red (high density). The scale saturates to white at the highest densities.

Table 1: Characteristics for Varied Metallicity Runs

Case	f_{κ}	a_{max}	t_1^a	t_2^a	$\langle A \rangle$	t_{cool}^a
$1/4 Z_{\odot}$	1/4	$1 \mu\text{m}$	N/A	N/A	1.04	3.5
$1/2 Z_{\odot}$	1/2	$1 \mu\text{m}$	4.0	10	0.82	5.0
Z_{\odot}	1.0	$1 \mu\text{m}$	5.0	10	0.78	5.5
$2 Z_{\odot}$	2.0	$1 \mu\text{m}$	5.0	10	0.52	6.6
1mm	1.0	1 mm	7.0	11	0.58	10.0

^aAll times are given in units of ORPs.